TITLE:

Statistical Analysis of Medium-Scale Traveling Ionospheric Disturbances Over Japan Based on Deep Learning Instance Segmentation

AUTHOR(S):

Liu, Peng; Yokoyama, Tatsuhiro; Fu, Weizheng; Yamamoto, Mamoru

京都大学学術情報リポジトリ
KURENAI 紅
Kyoto University Research Information Repository

京都大学
KYOTO UNIVERSITY

AGU ADVANCING EARTH AND SPACE SCIENCE

Space Weather®

Author Contributions:
Conceptualization: Peng Liu
Data curation: Peng Liu, Tatsuhiro Yokoyama
Formal analysis: Peng Liu, Weizheng Fu
Funding acquisition: Tatsuhiro Yokoyama, Mamoru Yamamoto
Investigation: Peng Liu, Tatsuhiro Yokoyama, Mamoru Yamamoto
Methodology: Peng Liu
Project Administration: Tatsuhiro Yokoyama, Mamoru Yamamoto
Resources: Peng Liu
Software: Peng Liu
Supervision: Tatsuhiro Yokoyama, Mamoru Yamamoto

Statistical Analysis of Medium-Scale Traveling Ionospheric Disturbances Over Japan Based on Deep Learning Instance Segmentation

Peng Liu[1] , Tatsuhiro Yokoyama[1] , Weizheng Fu[1] , and Mamoru Yamamoto[1]

[1]Research Institute for Sustainable Humanosphere, Kyoto University, Uji, Japan

Abstract Medium-scale traveling ionospheric disturbances (MSTIDs) are observed as parallelly arrayed wavelike perturbations of Total Electron Content (TEC) in ionospheric F region leading to satellite navigation error and communication signal scintillation. The observation method for MSTIDs, detrended TEC (dTEC) map, summarizes the perturbation component of TEC having the merits of full-time and two-dimensional. However, previous automatic processing methods for dTEC map cannot discriminate MSTIDs from other irregular ionospheric perturbations intelligently. With the development of artificial intelligence in recent years, deep learning approach is expecting to clarify the controversy of MSTID external dependence (season and solar/geomagnetic activity) under debating for decades. Therefore, this research proposes a real-time processing algorithm for dTEC maps based on Mask Region-Convolutional Neural Network (R-CNN) model of deep learning instance segmentation to detect wavelike perturbations intelligently with an accuracy of about 80% and a processing speed of about 8 fps. Then isolated perturbations are eliminated and only MSTID waveforms are chosen to obtain statistical characteristics of MSTIDs. With this algorithm, we analyzed up to 1,209,600 dTEC maps from 1997 to 2019 over Japan automatically and established a database of hourly averaged MSTID characteristics. This research introduces the partial correlation coefficient for the first time to clarify the solar/geomagnetic activity dependence of MSTID characteristics which is independent with each other.

Plain Language Summary Medium-scale traveling ionospheric disturbance (MSTID) is an ionospheric irregularity phenomenon observed as parallelly arrayed wavelike perturbations of Total Electron Content (TEC) with a period of less than 1 hr and wavelength of less than 500 km. The TEC is measured by the signal propagation delay between satellite and ground receiver network and its perturbation component is summarized in detrended TEC (dTEC) map as the observation method of MSTIDs. However, previous automatic processing methods for dTEC map cannot discriminate MSTIDs from other irregular ionospheric perturbations. The controversy of MSTID external dependence (season and solar/geomagnetic activity) has been under debating for decades in previous statistical analyses. To solve these problems, the first MSTID processing algorithm based on deep learning instance segmentation is proposed in this research to process up to 1,209,600 dTEC maps from 1997 to 2019 over Japan intelligently and automatically. The results clarify the external factor dependence of MSTID characteristics independently by introducing partial correlation coefficient. This statistical analysis of MSTIDs will contribute to the industrial deployment such as space weather forecast and quality improvement of satellite communication.

1. Introduction

The plasma density in the ionospheric F region keeps fluctuating in various temporal and spatial scales. The quasi-wavelike ionospheric disturbances are called as traveling ionospheric disturbances (TIDs), which can be further divided into small-scale TIDs (SSTIDs) (Yin et al., 2019), medium-scale TIDs (MSTIDs) and large-scale TIDs (LSTIDs) (Georges, 1968) by their scales. In terms of MSTIDs, since Sydney Radio Research Board first gave the experimental existence proof (Munro, 1950), observation methods for MSTIDs have been varying all the time (Evans et al., 1983; Jacobson et al., 1995) but the most common methods have been two-dimensional observation since 1990s due to the large observable range. One two-dimensional observation method, High Frequency (HF) radar (Samson et al., 1990), is mostly used to observe daytime MSTIDs. Another method, all-sky airglow imager was also proposed (Mendillo et al., 1997), but it can only work at nighttime because the intensity of atmospheric airglow is too low compared with that of sunlight. Besides, the completion of the first Global Navigation Satellite System (GNSS) in USA, Global Positioning System (GPS), made it possible to carry out

Validation: Peng Liu, Tatsuhiro
Yokoyama, Weizheng Fu
Visualization: Peng Liu
Writing – original draft: Peng Liu
Writing – review & editing: Peng Liu,
Tatsuhiro Yokoyama, Weizheng Fu

two-dimensional and low-cost observation for MSTIDs by GPS-TEC method (Calais & Minster, 1995). This method is full-time because the detrended Total Electron Content (dTEC) of the ionosphere above the ground receiver is derived from group delays (phase advances) of satellite signal whenever daytime or nighttime (Saito et al., 1998). Based on GPS-TEC method, this research utilizes from 1997 to 2019 up to 1,209,600 dTEC maps provided by Japanese GNSS Earth Observation Network (GEONET) to analyze MSTID characteristics at both daytime and nighttime.

Automatic analysis for dTEC maps is difficult because the composition of perturbations are complicated and mixed with each other: parallel-arrayed wavelike perturbations of MSTIDs, isolated wavelike perturbations, irregular ionospheric disturbances and point white noise. Previous processing methods in MSTID research for detrended GPS-TEC data can be divided into two categories: Time domain analyses, such as the ratio of TEC variation to TEC average $(\Delta I / \bar{I} > 1\%)$ (Kotake et al., 2006), percentage fractional TEC variation $(S > 0.05)$ (Kil & Paxton, 2017), are unable to distinguish MSTIDs and irregular TEC disturbances. Frequency domain analyses, such as Multi-channel Maximum Entropy Method (MMEM) (Ding et al., 2011), Fast Fourier Transform (FFT) (Hernández-Pajares et al., 2006), are unable to distinguish MSTIDs and isolated wavelike perturbations because the successive passage of isolated wavelike perturbations with different propagation directions also produces a similar frequency spectrum as MSTIDs. In this research, we propose the first MSTID processing algorithm based on deep learning instance segmentation which can detect MSTIDs intelligently and derive their characteristics automatically.

Although many statistical researches have analyzed MSTIDs, the solar and geomagnetic activity dependence of MSTIDs are still under debating. In terms of the solar activity dependence of nighttime MSTID occurrence, both positive correlation (Hernández-Pajares et al., 2006, 2012; Kil & Paxton, 2017) and negative correlation (Kotake et al., 2006; Martinis et al., 2010; Shiokawa, Ihara, et al., 2003) are revealed at mid/high latitude in previous researches. Recent research (Terra et al., 2020) suggests that it is associated with season when discussed in monthly level instead of annual level, specifically, positive correlation with occurrence rate of nighttime MSTIDs in summer but negative in winter. In terms of geomagnetic activity dependence of MSTID characteristics, the controversy of positive correlation (Terra et al., 2020), negative correlation (Seker et al., 2011) and uncorrelated conclusion (Saito et al., 2001) exist. The variation of MSTID characteristics is influenced by multiple external factors synthetically, so that the correlation coefficient used in previous researches is not independent. In this research, the partial correlation coefficient in statistics, which can eliminate inter-factor influence, is introduced to determine the dependence of each external factor for MSTID characteristics independently instead of traditional correlation coefficient.

2. Data Set

The GEONET in Japan composed of about 1,300 GNSS ground receivers with a spatial distribution shown in Figure 1a, has been running since October 1994. With the GPS-TEC data provided by GEONET, Saito et al. (1998) found that after a running average detrending procedure, the wave structures of MSTIDs are clearly visible in the dTEC map as shown in Figure 1b. In this research, we follow the same procedure and set the detrending window as 1 hr, which will subtract an average of ±30 min to eliminate the influence of long-term TEC variation because previous multi-methods (Frissell et al., 2014; Huang et al., 2016) suggest that the maximum period of MSTIDs is shorter than 1 hr. However, it is hard to clarify a boundary between the crest and trough of MSTIDs in a cloud point map, which brings trouble to the next step when the deep learning network learns the feature of MSTIDs, so that the spatial smoothing procedure of nearby 3 × 3 pixels is taken to get continuous dTEC maps as shown in Figure 1c. Considering the dTEC derived from paths with a low elevation angle contain errors associated with cycle slips and multi-path fading, the satellite signals with zenith angles larger than 55° are eliminated as shown in Figure 1d.

The dTEC maps are drawn every 10 min and uploaded to the website of National Institute of Information and Communications Technology (NICT). Total number reaches 1,209,600 images from 1997 to 2019 in the same 368 × 396 pixel resolution and 0.15° × 0.15° spatial resolution within the area of 124°–148°E longitude and 24°–48°N latitude at 300 km ionospheric mapping shell altitude (Otsuka et al., 2021). Considering the different patterns (extension and propagation direction) of daytime and nighttime MSTIDs, we divide dTEC maps into

AGU
ADVANCING EARTH
AND SPACE SCIENCE
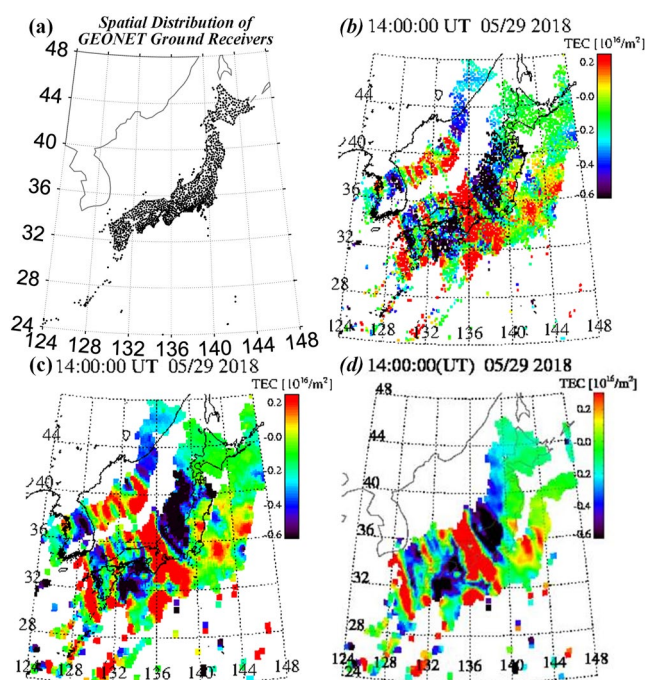
Figure 1. (a) The spatial distribution of GNSS Earth Observation Network (GEONET) ground receivers. (b) The point cloud map of detrended TEC (dTEC). (c) The dTEC map after the spatial smoothing of nearby 3×3 pixels. (d) The dTEC map after eliminating satellite signals with zenith angles larger than $55°$.

two groups according to local time (LT = UT + 9): daytime is defined as 7:00–18:50 (LT), the rest is grouped as the nighttime data set.

There is no standard data set with ground truth for the deep learning detection of MSTIDs. In this research, we propose the first MSTID detection data set which contains 3,000 dTEC maps in total with label images as ground truth. According to observation time, they are divided into daytime and nighttime groups equally and all the 1,500 images of each data set are selected randomly. We manually annotate all wavelike perturbations by open-source software *Labelme*, where crests and troughs of MSTIDs are annotated as red and blue respectively, and background, white noise or non-wavelike perturbations are annotated as green. Although contents of datasets are selected randomly, we review them to ensure that they are representative and not homogeneous.

Daytime and nighttime data sets are further grouped by three different usages: training data set, validation data set, and test data set. Training data set is used for deep learning network model training. Validation data set is used for model loss validation after training is partially completed to adjust the hyperparameters of subsequent training procedure such as learning rate. Test data set is used for model accuracy evaluation after the training is completely finished. The image number portion ratio of three branch datasets is 10:2:3 for both daytime and nighttime datasets.

3. Analysis Method

Figure 2 shows the analysis procedure of this research: the deep learning instance segmentation network, Mask Region-Convolutional Neural Network (R-CNN) model, is used to detect wavelike perturbations intelligently. Then the circumscribed ellipses are drawn to normalize the detected wavelike structures. The discrimination whether a wavelike structure belongs to a MSTID can be accomplished by filtering criterion based on the spatial distribution features of MSTIDs. To avoid the situation that a wavelike structure is denied to be a part of MSTID just because of several anomalous characteristics, the nonlinear optimization tool is used to determine the threshold of filtering criterion. Finally, with the filtering criterion eliminating isolated wavelike disturbances as shown in
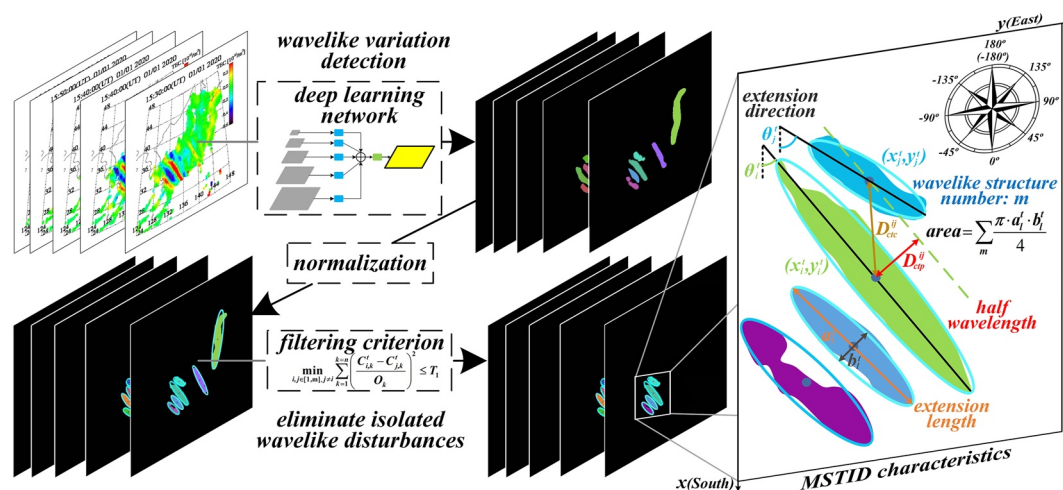
Figure 2. The flow chart of the algorithm proposed in this research. Note that the coordinate system of this research is inherited from OpenCV library. Wavelength is normalized as average center to projection distance D_{ctp}. Center to center distance D_{ctc} is only used as spatial distribution constraint to determine the threshold of filtering criterion.

京都大学
KYOTO UNIVERSITY

AGU
ADVANCING EARTH
AND SPACE SCIENCE

Space Weather

10.1029/2022SW003151

京都大学学術情報リポジトリ
KURENAI 紅
Kyoto University Research Information Repository
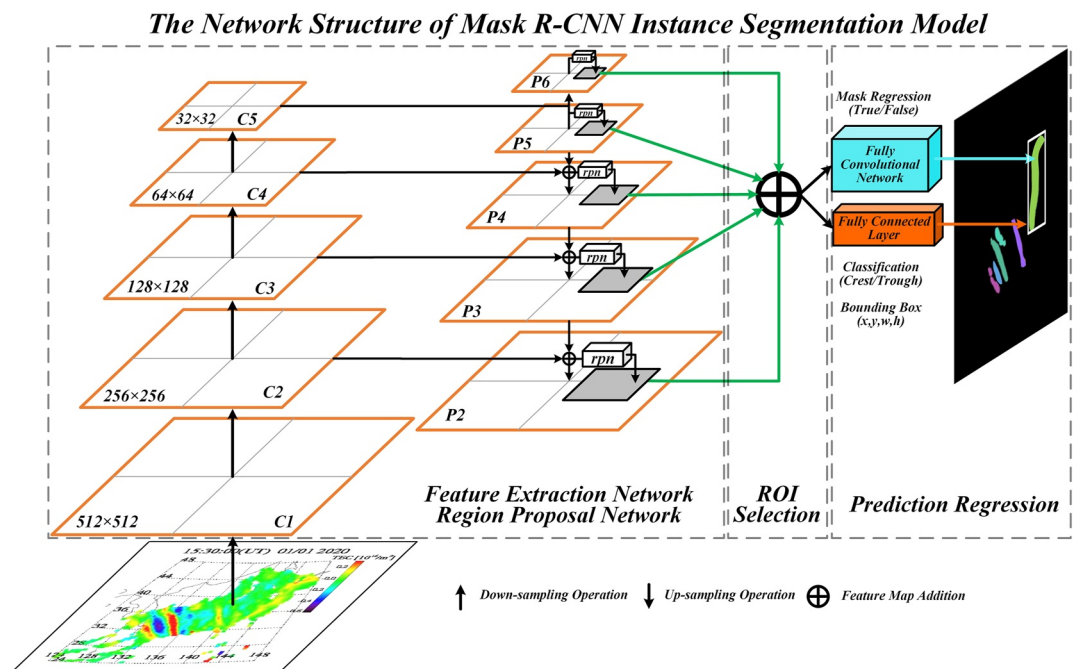
Figure 3. The network structure of Mask R-CNN instance segmentation model contains the feature extraction network, Region Proposal Network (RPN), Region of Interest (ROI) selection then normalization and the prediction regression. The upward and downward arrows in the feature extraction network (C_1–C_5 and P_2–P_6 feature maps) represent the down-sampling and up-sampling with a stride of 0.5 and 2, respectively.

the left part of Figure 2, MSTID characteristics are derived automatically as shown in the right part of Figure 2. Details are further discussed in the following subsections.

3.1. Wavelike Structure Detection

Traditional deep learning convolutional networks (Krizhevsky et al., 2012) are unsuitable for MSTID detection because these networks only output one overall classification prediction for a whole input image, which is image-level recognition due to the existence of fully connected layer. Long et al. (2015) proposed a new Fully Convolutional Network (FCN) structure without fully connected layer which can classify every pixel by outputting a mask image consisting of different colors in which one same color refers to one same category. This pixel-level recognition method, so-called semantic segmentation, ignores spatial information of different individuals that belong to the same category, which is fatal to the postprocess of MSTID characteristic derivation. Then a new branch of deep learning, so-called instance segmentation implemented by Mask R-CNN (He et al., 2017), which not only classifies the category of every image pixel but also annotates different individuals in the same category with different colors, constitutes the theoretical basis of the automatic detection of wavelike perturbations in this research.

Figure 3 shows the overall architecture of Mask R-CNN, which can be divided into 4 parts: feature extraction network, region proposal network, Region of Interest (ROI) selection and normalization, and finally the prediction regressions for bounding box, classification and mask.

- Feature extraction network: the Feature Pyramid Network (FPN) structure is deployed as the feature extraction network, which is composed of 5 down-top stages ($C_1 \rightarrow C_5$ feature maps) in deep residual network backbone (ResNet-50/ResNet-101) and their top-down lateral connections ($P_6 \rightarrow P_2$ feature maps) (Lin et al., 2017).
- Region Proposal Network (RPN): three anchor bounding boxes with different width-height ratio ($w/h = 0.5/1.0/2.0$) centered on each pixel of P_2–P_6 feature maps are pre-generated. According to the ground truth of bounding box provided by the label image, RPN learns features of positive (wavelike structure exists) and negative (not exists) anchor boxes and knows how to sample positive bounding box which is called as ROI after the model training procedure.

- ROI selection and normalization: one ROI can be generated by any feature map of P_2–P_6, Mask R-CNN selects its corresponding feature map P_k according to size of ROI ($w \times h$) by the formula: $k = \left[4 + \log_2 \sqrt{wh}/224 \right]$, where [ ] refers to the nearest integer function (Lin et al., 2017). For example, when ROI size equals to the standard ImageNet input size 224×224, Mask R-CNN chooses P_4 to segment the wavelike structure. ROIs with different sizes obtained from different stages ($P_2 - P_6$) are further normalized to the same fixed size feature map by ROI Align (7×7 for bounding box or classification regression and 14×14 for mask regression).
- Prediction regression: above two kinds of normalized feature maps within the same ROI are input into traditional CNN branch with fully connected layer and FCN branch without fully connected layer for image-level bounding box/classification and pixel-level mask prediction regressions, respectively.

The ROI loss function L_{ROI} used for prediction regression consists of multi-class classification cross-entropy loss L_{cls}, box regression smooth L_1 loss L_{box} (Girshick, 2015) and mask binary cross-entropy loss L_{mask} (He et al., 2017) as shown by formula 1, here the symbols with hat refer to the network prediction results and those without hat refer to the label ground truth. p_i is the classification probability of the ROI for i_{th} class of total N_{cls} class. The balance hyperparameter λ equals to 1 in Mask R-CNN. The tuple $t = (x, y, w, h)$ records the center pixel coordinate, width and height of the bounding box. Boolean variable y_{mn} is 1 if (m, n) pixel corresponds to the mask pixel of the wavelike structure or 0 for the background in ROI with a total size of $N_{pix} \times N_{pix}$. Note that L_{cls} equals to $- \log \hat{p}_u$ for true class u and 0 otherwise.

$$L_{ROI} = L_{cls} + L_{box} + L_{mask} = -\frac{1}{N_{cls}} \sum_{i=0}^{N_{cls}} p_i \log \hat{p}_i + \lambda \sum_{\substack{i \in \\ \{x,y,w,h\}}} \begin{cases} 0.5(\hat{t}_i - t_i)^2, \text{if } |\hat{t}_i - t_i| < 1 \\ |\hat{t}_i - t_i| - 0.5, \text{otherwise} \end{cases}$$
$$-\frac{1}{N_{pix}^2} \sum_{m,n=1}^{N_{pix}} \left[y_{mn} \log \hat{y}_{mn} + (1 - y_{mn}) \log(1 - \hat{y}_{mn}) \right] \tag{1}$$

The transfer learning deployment is adopted in this research, where the Mask R-CNN model is pre-trained by COCO data set with more than 200,000 images and 80 object categories to obtain a basic model weight for the target detection. The sampled region ratio of positive (wavelike structure exists) to negative (not exists) is 1:3 for both categories (crest and trough) in a dTEC map. We deploy the same model training parameters as Mask R-CNN (He et al., 2017) for a controlled experiment with an initial learning rate of 0.02, sampled ROI of 512, weight decay of 0.0001 and momentum of 0.9.

Figure 4 shows the learning curves which are the ROI loss variation of training (red) and validation (blue) datasets in the training procedure of 100 epochs when using the ResNet-50/ResNet-101 network backbones and daytime/nighttime datasets. The horizontal axis epoch refers to the the iteration number that the learning algorithm works through the entire training data set with the data augmentation (shuffling and resizing) between different iterations. In all circumstances, both the learning curves of training and validation datasets start from a close ROI loss at the first epoch for about 2.5, which suggests a good randomness of the dTEC map datasets. The learning curves of validation data set (blue curve) fluctuates more drastically compared with that of training data set (red curve) because only the training data set participates in the training procedure. Compared with ResNet-50 backbone (Figures 4a and 4b), the loss gradient descent speed of ResNet-101 backbone (Figures 4c and 4d) is quicker for both daytime and nighttime datasets which suggests a deeper network has a better feature extraction ability corresponding with the conclusion of previous research (He et al., 2017). Meanwhile, the converged ROI loss between training and validation datasets at the 100_{th} epoch for ResNet-101 backbone (Figures 4a and 4b) are closer compared with that of ResNet-50 backbone (Figures 4c and 4d), which suggests that the model overfitting phenomenon occurring in the training procedure is alleviated due to the better feature extraction ability. Compared with nighttime data set (Figures 4b and 4d), the loss variance between training and validation datasets of daytime data set (Figures 4a and 4c) is larger because the amplitude of daytime MSTIDs is smaller than that of nighttime MSTIDs (Ding et al., 2011) and there are more non-wavelike TEC perturbations at daytime making it more difficult to discriminate daytime MSTIDs and more likely to be overfitting. The ROI loss converges in 100 training epochs where the models with the minimum loss in the validation data set for all circumstances are used for the evaluation of wavelike structure detection in Section 4.

<pre>
</pre>

Learning Curve in the Training Procedure for 100 Epochs
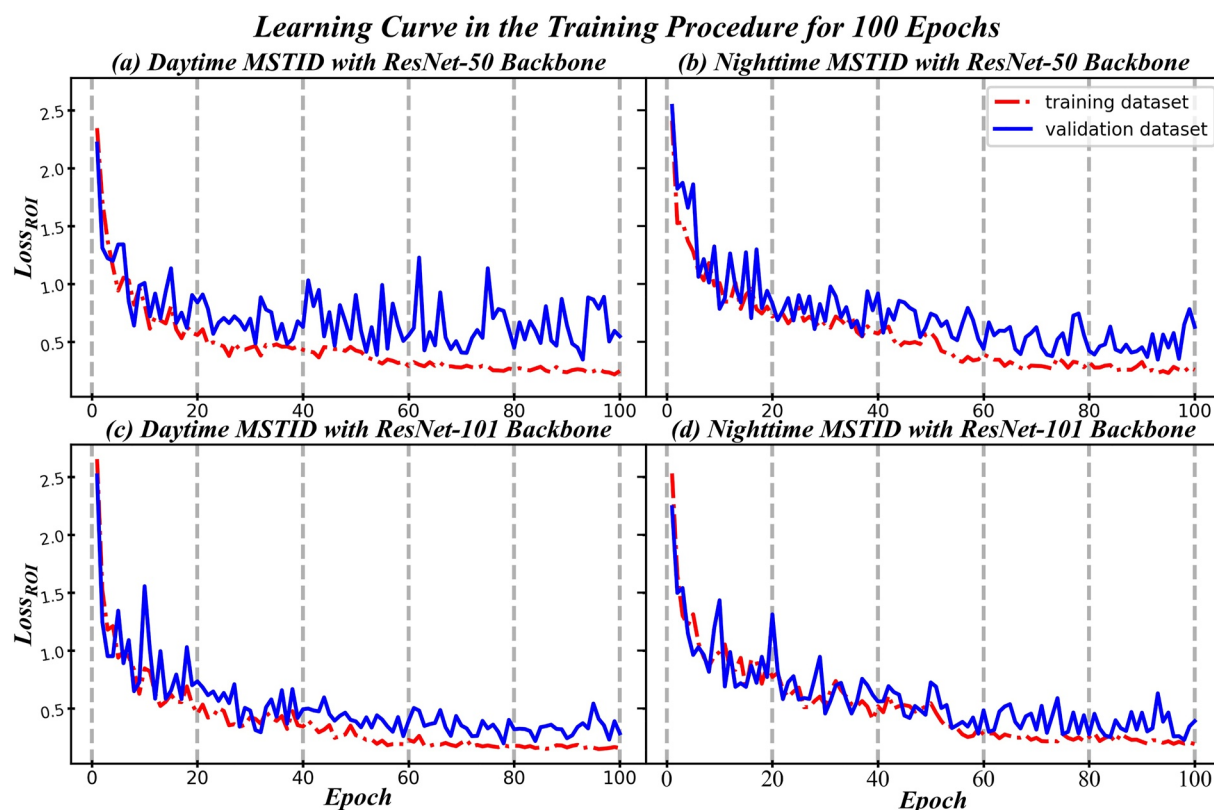
Figure 4. The learning curve between epoch and Region Of Interest (ROI) loss in the training procedure with the training (red) and validation (blue) datasets under different circumstances: (a) Daytime Medium-scale traveling ionospheric disturbances (MSTIDs) with ResNet-50 backbone, (b) Nighttime MSTIDs with ResNet-50 backbone, (c) Daytime MSTIDs with ResNet-101 backbone, (d) Nighttime MSTIDs with ResNet-101 backbone.

3.2. Geometric Shape Normalization

The irregular edges and different shapes of wavelike perturbations detected by the deep learning instance segmentation will bring difficulties to the outlier elimination and characteristic derivation. In this case it is imperative to normalize the geometric shape of wavelike perturbations. In traditional object detection field, the way to annotate a target is drawing a circumscribed rectangle (bounding box) parallel to the image edge. However, this method is unsuitable for wavelike perturbations which will make many pixels pseudo annotated leading to large error when we calculate the area of MSTID waveforms. Instead, we draw a much closer geometry figure, circumscribed ellipse, for every wavelike structure based on the least squared ellipse fitting method provided by OpenCV open-source library to normalize the geometric shape of wavelike perturbations.

To quantify these wavelike perturbations mathematically, we inherit the same definition of pixel coordinate system from OpenCV Library shown in the right part of Figure 2, which is obtained by 90° clockwise rotation from traditional Cartesian coordinate system. To derive the MSTID wavelength, the central coordinate of the target wavelike structure is assumed as (x_i, y_i) with a major axis declination θ_i, then draw a parallel line to the major axis that crosses the center (x_j, y_j) of the next wavelike structure. The equation of this parallel line is written as: $y - y_j = \tan\theta_i(x - x_j)$. After transforming to the general form of straight line equation: $\tan\theta_i x - y + (y_j - \tan\theta_i x_j) = 0$, the center to projection distance D_{ctp} can be calculated by a point-to-line formula as:

$$D_{ctp}^{ij} = \frac{|\tan\theta_i x_i - y_i + y_j - \tan\theta_i x_j|}{\sqrt{(\tan\theta_i)^2 + (-1)^2}} \tag{2}$$

MSTID wavelength is assumed as the translational displacement, which is the average center to projection distance D_{ctp} instead of center to center Euclidean distance D_{ctc} shown in the right part of Figure 2 because D_{ctc} is the combined result of translation, rotation and deformation.

3.3. Isolated Wavelike Perturbation Elimination

Based on the coordinate system mentioned in last subsection, all wavelike perturbations in a dTEC map can be expressed by the following characteristic matrix $C_{m\times n}^t$:

$$C_{m\times n}^t = \begin{bmatrix} x_1^t & y_1^t & a_1^t & b_1^t & S_1^t & \cdots & \theta_1^t \\ x_2^t & y_2^t & a_2^t & b_2^t & S_2^t & \cdots & \theta_2^t \\ \vdots & \vdots & \vdots & \vdots & \vdots & \ddots & \vdots \\ x_m^t & y_m^t & a_m^t & b_m^t & S_m^t & \cdots & \theta_m^t \end{bmatrix} \tag{3}$$

The total row number m equals to the total number of wavelike perturbations, n refers to the total number of characteristics and t refers to the timestamp of the current dTEC map. For a certain wavelike structure, which refers to i_{th} row in $C_{m\times n}^t$, a 6-dimension characteristic vector ($n = 6$), that is, central coordinates (x, y), ellipse major/minor axis length (a, b), area S and declination of major axis θ, is used to represent one wavelike structure in this research. More characteristics can be accommodated by expanding the characteristic matrix if need.

Wavelike structure is only a necessary but insufficient condition for MSTID waveform determination. Isolated wavelike perturbations should be eliminated from mask images. If regarding characteristic row vector of a wavelike structure as a point in n-dimension space, the cross-correlation between different i_{th} and j_{th} wavelike perturbations can be measured by the following filtering criterion which can be expressed as the minimum weighted n-dimension Euclidean distance FC_i should be less than a threshold T_1:

$$FC_i = \underset{i,j\in[1,m],j\neq i}{\text{minimize}} \sum_{k=1}^{n} \left(\frac{C_{i,k}^t - C_{j,k}^t}{O_k} \right)^2 \leq T_1 \tag{4}$$

Here O_k is a scale normalization term, which refers to the magnitude order of k_{th} characteristic to avoid a characteristic with a greater magnitude order having larger influence on threshold T_1. For i_{th} ($i \in [1, m]$) row normalized wavelike structure in the processing dTEC map: if existing j ($j \in [1, m]$, $j \neq i$) satisfies the filtering criterion, we regard that i_{th} and j_{th} wavelike perturbations are a matching pair and belong to the same MSTID. On the contrary, we regard i_{th} wavelike structure as an isolated wavelike structure and is eliminated from mask image and characteristic matrix. After finishing the process for all iterations of i ($i \in [1, m]$), the remaining wavelike perturbations in the characteristic matrix can be regarded as MSTID waveforms.

3.4. Filtering Criterion Threshold

In order to figure out the exact value of threshold T_1, we refer to previous MSTID observation results (Garcia et al., 2000; Huang et al., 2018; Shiokawa, Ihara, et al., 2003), which suggest the range of MSTID wavelength is 100–500 km. MSTID wavelength is equivalent to the twice of D_{ctp} between spatially nearest crest and trough. To avoid an extreme situation of a small D_{ctp} and large D_{ctc} occurring when the center of another waveform is on the same long axis extension line of the target waveform, we also constrain that D_{ctc} should be smaller than a wavelength of 500 km. The difference of declination angle among different waveforms within a MSTID should be less than 30° both on spatial (Makela et al., 2010) and temporal (Ding et al., 2004) scale. Extension length difference among different waveforms within a MSTID is less than 300 km limited by the observable region. The wavelength variation of different waveforms in the same MSTID is less than 100 km (Huang et al., 2018) so that the waveform width difference should be less than 50 km. With above two constraints, the area difference should be less than 20,000 km². These constraints can be expressed as the following optimization problem:

$$\underset{x,y,a,b,\theta}{\text{maximize}} \quad FC_i = \left(\frac{x_i - x_j}{100}\right)^2 + \left(\frac{y_i - y_j}{100}\right)^2 + \left(\frac{a_i - a_j}{100}\right)^2 + \left(\frac{b_i - b_j}{50}\right)^2 + \left(\frac{\theta_i - \theta_j}{10}\right)^2$$

$$\text{subject to} \quad D_{ctp}^{ij} = \frac{|\tan\theta_i x_i - y_i + y_j - \tan\theta_i x_j|}{\sqrt{(\tan\theta_i)^2 + (-1)^2}} < 250, \quad \theta_i \neq \pm 90°,$$

$$D_{ctc}^{ij} = \sqrt{(x_i - x_j)^2 + (y_i - y_j)^2} < 500, \quad 0 < x, y < 3000,$$

$$|S_i - S_j| = \frac{|\pi(a_i b_i - a_j b_j)|}{4} < 20000, 0 < S < 50000,$$

$$50 < |x_i - x_j| < 500, \quad 0 < x < 3000,$$

$$50 < |y_i - y_j| < 500, \quad 0 < y < 3000,$$

$$|a_i - a_j| < 300, \quad 0 < a < 500,$$

$$|b_i - b_j| < 50, \quad 0 < b < 250,$$

$$|\theta_i - \theta_j| < 30° \quad 0 < \theta < 180°$$

(5)

After transforming to standard formation of nonlinear programming solver *fmincon* provided by *Matlab* optimization toolbox, where the objective function is multiplied by −1, the nonlinear multi-variable object function has an optimal solution for threshold T_1 which is *fval* = −39.7659 referring to the optimization result with an opposite symbol. The *exitflag* = 1 refers that first order optimality measure is less than the tolerance meeting the requirement. Compared with filtering out the waveform by constraint of each characteristic successively, the nonlinear optimization has stronger robustness.

4. Method Evaluation

In order to evaluate the accuracy of Mask R-CNN on test datasets, we adopt the Intersection over Union (IoU) metric, which calculates intersection and union pixel number between the prediction masks output by Mask R-CNN and the label images drawn manually. If the IoU of a predicted wavelike structure between the mask image and the label image is greater than 50%, this prediction is called as a True Positive (TP). Similarly, False Positive (FP) means that network outputs a wrong wavelike structure prediction which is not annotated in the label image (IoU ≤50%), False Negative (FN) refers to a missing detection which is indeed labeled manually (IoU ≤50%). Following the routine accuracy evaluation method in machine learning field (Chinchor, 1992), we evaluate the accuracy of our model in test data set from two standard measurement metrics: F_1 (or F) score and AP_{50} (or mAP) defined as the above formula where N means total object categories referring to the crest and trough in this research.

$$\begin{cases} F_1 = \frac{1}{N}\sum_N \frac{2TP}{2TP + FN + FP} \\ AP_{50} = \frac{1}{N}\sum_N \frac{TP}{TP + FP} \end{cases}$$

(6)

After Mask R-CNN models with ResNet-50 or ResNet-101 feature extraction backbone have been trained on the training and evaluation datasets, we evaluate the F_1 and AP_{50} accuracy scores and average frames per second (*fps*) speed on RTX3090 GPU or i5-8400 CPU for daytime and nighttime test datasets, respectively. The results are shown in Table 1. In terms of detection accuracy, the F_1 and AP_{50} of ResNet-101 backbone is higher compared with ResNet-50 backbone due to the better feature extraction ability for the deeper network structure. In terms of process speed, the model with ResNet-101 backbone is slower compared with ResNet-50 backbone due to the deeper convolution layers, so that the computational complexity for the model with ResNet-101 backbone is higher. However, considering the update interval of GPS-TEC data is 30 s, the algorithm of this research is real-time whenever processed on i5-8400 CPU or RTX3090 GPU.

Figure 5 shows the processing result for dTEC maps (Figure 5a) in the test data set under different circumstances, such as dense/sparse MSTID waveform, white noise or satellite data error attaching produced by satellites with

Table 1
The Wavelike Structure Detection Result (Detection Accuracy in Different ResNet-50/ResNet-101 Network Backbone and Process Speed in RTX3090 GPU or i5-8500 CPU Devices) of Mask R-CNN Instance Segmentation Model

| Data set	Backbone	Detection accuracy/%	Process speed/fps
Daytime Test	ResNet-50	F_1: 71.62, AP_{50}: 73.85	GPU: 8.24, CPU: 1.14
	ResNet-101	F_1: 76.94, AP_{50}: 82.61	GPU: 7.54, CPU: 1.03
Nighttime Test	ResNet-50	F_1: 74.11, AP_{50}: 77.18	GPU: 7.95, CPU: 1.11
	ResNet-101	F_1: 80.57, AP_{50}: 79.32	GPU: 7.46, CPU: 0.98

low elevation angle. The output of Mask R-CNN (Figure 5c) is very close to the ground truth (Figure 5b). The failure detection always happens when the size of the missed wavelike structure is much smaller than others shown by the third wavelike structure from the left side of case 2 ground truth label. Meanwhile, it is difficult to improve the detection accuracy to nearly 100% due to the subjectivity of manual annotation in label image, for example, the discrimination whether the first narrow wavelike structure from the right side of case 3 ground truth label is a wavelike structure or not is a subjective matter. Figure 5d shows the circumscribed ellipse normalization
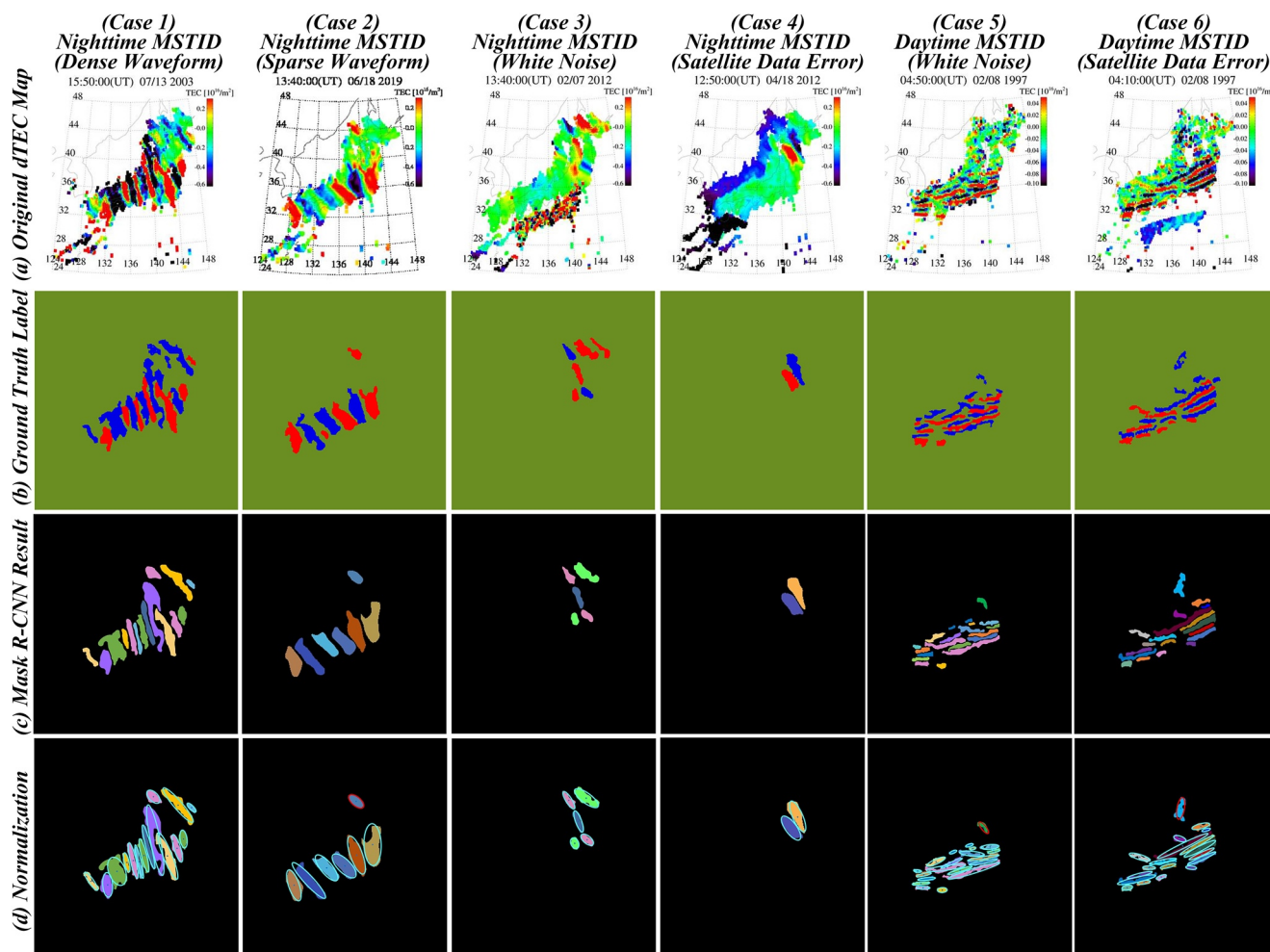
Figure 5. The original detrended Total Electron Content (dTEC) maps (row a), manually annotated Ground Truth label images used for supervised learning (row b), the instance segmentation results of Mask R-CNN model (row c) and circumscribed ellipse normalization result (row d) the under different circumstances: nighttime Medium-scale traveling ionospheric disturbance (MSTID) with dense waveforms (case 1), nighttime MSTID with sparse waveforms (case 2), nighttime MSTID with the white noise (case 3), nighttime MSTID with the satellite data error (case 4), daytime MSTID with the white noise (case 5) and daytime MSTID with the satellite data error (case 6).

Parallel Coordinates Plot for Characteristic Matrix and Filtering Criterion of Wavelike Structures in Figure 5
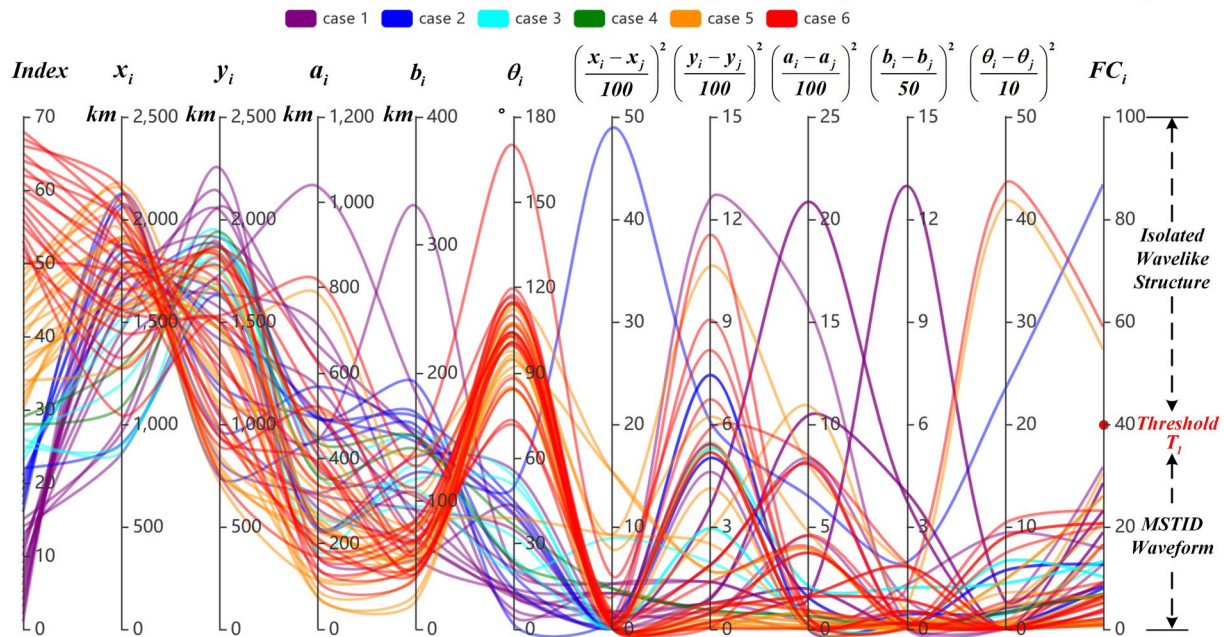
Figure 6. The parallel coordinates plot for characteristic matrix and filtering criterion of all wavelike structures in Figure 5. Each line represents a wavelike structure and different colors refer to different cases. The filtering criterion $FC_i < T_1$ can discriminate isolated wavelike structures (the top three wavelike structure in the cases 2, 5, and 6 of Figure 5) from Medium-scale traveling ionospheric disturbance (MSTID) waveforms (others).

result where wavelike structures annotated by blue ellipses are regarded as MSTID waveforms meeting the filtering criterion $FC_i < T_1$ while those annotated by red ellipses are discriminated as isolated wavelike structures ($FC_i > T_1$).

Figure 6 shows the algorithm performance of the isolated wavelike perturbation elimination with the filtering criterion $FC_i < T_1$ for all wavelike structures detected by Mask R-CNN in Figure 5d which are indexed as No. 1–29 for cases 1–4 nighttime MSTIDs and No. 30–68 for cases 5–6 daytime MSTIDs. Parallel coordinates from x_i to θ_i and from $(x_i - x_j)/100$ to $(\theta_i - \theta_j)/10$ refer to each component of i_{th} wavelike structure characteristic vector C_i and each component of the weighted n-dimension Euclidean distance FC_i between their matching j_{th} wavelike structure, respectively. It is obvious that the threshold T_1 determined by the nonlinear optimization method $T_1 = 39.7659$ can discriminate isolated wavelike structures (the top three wavelike structures in the cases 2, 5 and 6 of Figure 5d) from MSTID waveforms (others). Meanwhile, it is obvious that the extension direction θ_i is the only coordinate that daytime (cases 5–6) and nighttime (cases 1–4) MSTIDs are distinct from each other.

5. Analysis Result

1,209,600 dTEC maps over Japan with a sample interval of 10 min from 1997 to 2019, are provided into Mask R-CNN instance segmentation model with ResNet-101 backbone. The instantaneous characteristics of MSTIDs are estimated with the same interval of 10 min by the algorithm proposed in this research, so that a characteristic database of MSTIDs over Japan is constructed.

Table 2 shows the statistical features of monthly averaged analysis results (mean, minimum and maximum) of each MSTID characteristic for 23 years. Besides, to determine the solar and geomagnetic activity dependence of annually averaged MSTID characteristics independently, we calculate the partial correlation coefficient $r'_{ij/h}$ shown as formula 7 where E refers to expected value operator (Ellett & Ericson, 1986), instead of traditional correlation coefficient r_{ij} between MSTID characteristics C and solar activity $F_{10.7}$ (geomagnetic activity Kp) index which can eliminate the influence of geomagnetic (solar) activity for $r'_{C \cdot F_{10.7}/Kp}$ $\left(r'_{C \cdot Kp/F_{10.7}} \right)$ shown in Table 2. Same with the correlation coefficient, partial correlation coefficient also take a value between $[-1,0]$

京都大学
KYOTO UNIVERSITY

A Self-archived copy in
Kyoto University Research Information Repository
https://repository.kulib.kyoto-u.ac.jp

京都大学学術情報リポジトリ
KURENAI 紅
Kyoto University Research Information Repository

Table 2
The Statistical Features of Monthly Averaged Analysis Results (Mean, Minimum and Maximum) and the External Factor Dependence of Annually Averaged MSTID Characteristics (Solar/Geomagnetic Activity and Seasonal Dependence)

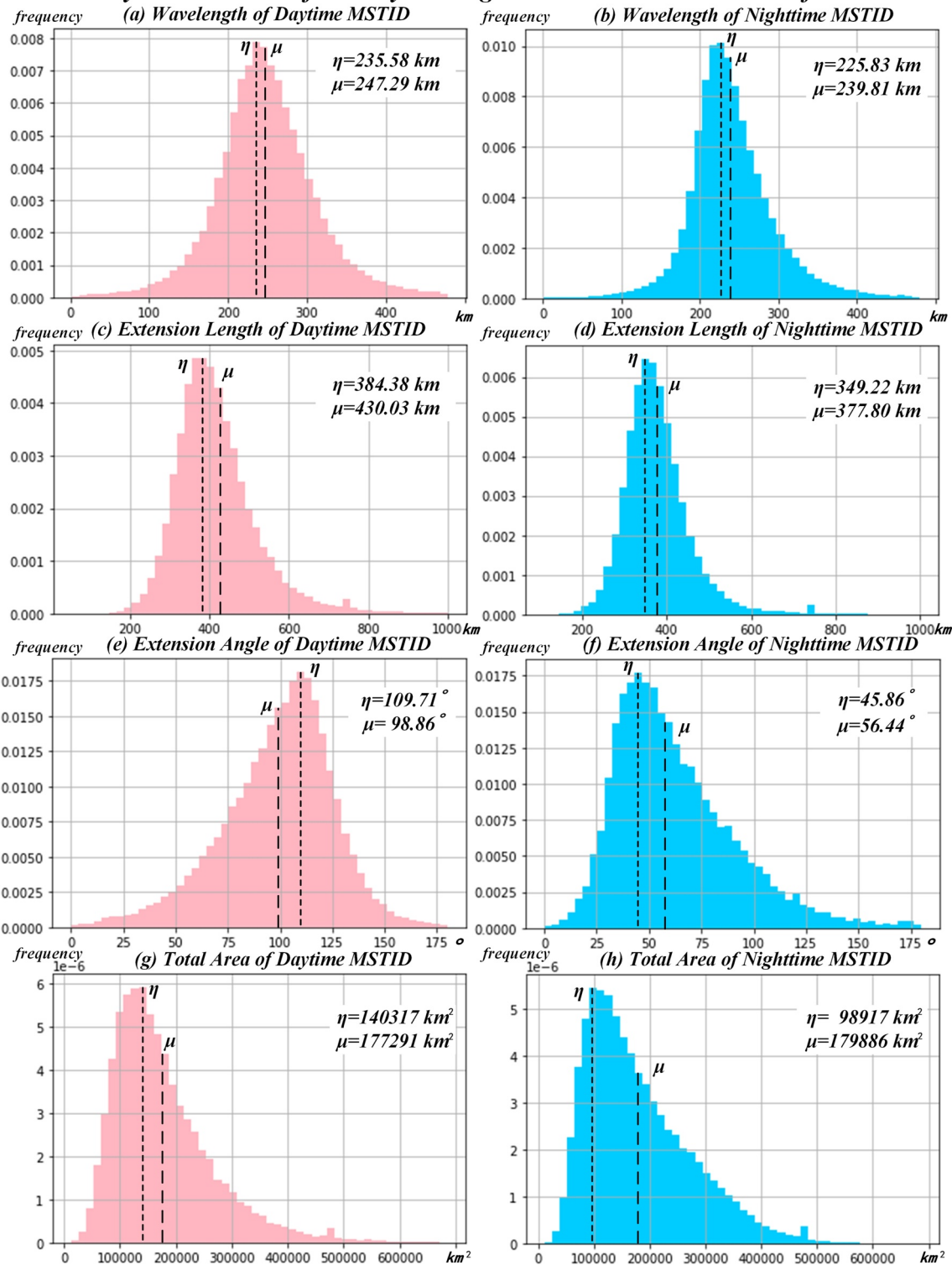| Time	Characteristic/unit	Mean	Minimum Maximum	Solar Activity Dependence	Geomagnetic Dependence	Seasonal Dependence
Daytime	Occurrence Rate/%	34.82	3.01	Winter:0.254	r': 0.246	Max: Winter, Submax: Summer
			79.26	Spring: −0.467	Not Obvious	Min: Spring,Submin: Autumn
	Wavelength/km	247.29	217.74	r': −0.848	r': 0.241	Max: Autumn,Submax: Spring
			272.59	Negative	Not Obvious	Min: Summer,Submin: Winter
	Extension Direction/°	98.86	84.33	r': 0.361	r': 0.123	Max: Winter,Submax: Summer
			113.08	Not Obvious	Not Obvious	Min: Spring,Submin: Autumn
	Extension Length/km	430.03	365.43	r': 0.613	r': 0.254	Max: Winter,Submax: Summer
			481.59	Positive	Not Obvious	Min: Spring,Submin: Autumn
	Wave Number/none	2.84	2.25	r': 0.491	r': 0.129	Max: Winter,Submax: Summer
			4.19	Positive	Not Obvious	Min: Spring,Submin: Autumn
	Total Area/km^2	1,77,291.58	1,29,766.63	r': 0.583	r': 0.175	Max: Winter,Submax: Summer
			2,71,744.56	Positive	Not Obvious	Min: Spring,Submin: Autumn
Nighttime	Occurrence Rate/%	53.38	6.81	Summer: 0.351	r': 0.299	Max: Summer,Submax: Winter
			97.68	Winter:−0.741	Not Obvious	Min: Autumn,Submin: Spring
	Wavelength/km	239.81	220.20	r': −0.522	r': −0.278	Max: Autumn,Submax: Spring
			264.03	Negative	Not Obvious	Min: Summer,Submin: Winter
	Extension Direction/°	56.44	37.98	r': 0.928	r': 0.391	Max: Summer,Submax: Winter
			67.46	Positive	Not Obvious	Min: Autumn,Submin: Spring
	Extension Length/km	377.80	326.76	r': 0.846	r': 0.255	Max: Summer,Submax: Winter
			405.73	Positive	Not Obvious	Min: Autumn,Submin: Spring
	Wave Number/none	3.41	2.17	r': −0.742	r': 0.263	Max: Summer,Submax: Winter
			5.88	Negative	Not Obvious	Min: Autumn,Submin: Spring
	Total Area/km^2	1,79,886.40	96,384.84	r': 0.426	r': 0.171	Max: Summer,Submax: Winter
			3,00,508.76	Positive	Not Obvious	Min: Autumn,Submin: Spring

for negative correlation or [0,1] for positive correlation and a larger absolute value represents more significant the correlation is. It is obvious that MSTID characteristics follow a significant correlation with solar activity $\left(r'_{C \cdot F_{10.7}/Kp} > 0.3 \right)$ but no obvious correlation with geomagnetic activity $\left(r'_{C \cdot Kp/F_{10.7}} < 0.4 \right)$.

$$
\begin{cases}
r_{ij} & = \dfrac{E(ij) - E(i)E(j)}{\sqrt{E(i^2) - E(i)^2}\sqrt{E(j^2) - E(j)^2}} \\
r'_{ij/h} & = \dfrac{r_{ij} - r_{ih}r_{jh}}{\sqrt{\left(1 - r_{ih}^2\right)\left(1 - r_{jh}^2\right)}}
\end{cases}
\tag{7}
$$

Figure 7 shows the probability distribution histograms of hourly averaged MSTID characteristics for 23 years excluding the discrete characteristics. The vertical axis frequency is viewed as the probability for each characteristic value and its range is divided into 50 bins as the horizontal axis. The maximum likelihood value η and the mean value μ are annotated in each histogram. According to Figures 7a and 7b, the mean wavelength is corresponding with previous observations (Hernández-Pajares et al., 2012). The possible physical explanation based on gravity wave theory for daytime MSTID wavelength is that only when the horizontal wavelength is greater than 200 km, the gravity wave can propagate upward to the MSTID occurrence altitude of 300 km (Vadas, 2007). Previous inter-layer E-F coupling simulation for nighttime MSTID wavelength is also about 200 km (Yokoyama

Figure 7. The probability distribution histograms of annually averaged Medium-scale traveling ionospheric disturbances (MSTID) continuous characteristics from 1997 to 2019 including wavelength (a/b), extension direction (c/d), extension length (e/f) and total area (g/h) for daytime (red) and nighttime (blue). The vertical axis frequency is viewed as the probability for each characteristic value and its range is divided into 50 bins as the horizontal axis. The maximum likelihood value η, which is the midpoint on the horizontal axis of the highest frequency bin, and the average value μ are annotated in each histogram.

京都大学
KYOTO UNIVERSITY

AGU
ADVANCING EARTH
AND SPACE SCIENCE

Space Weather

10.1029/2022SW003151

京都大学学術情報リポジトリ
KURENAI 紅
Kyoto University Research Information Repository

& Hysell, 2010). The maximum of of hourly averaged MSTID wavelength is indeed less than 500 km corresponding to the wavelength constraint in threshold T_1 determination of the filtering criterion, which proves the effectiveness of nonlinear optimization method. Moreover, the average of extension direction of daytime and nighttime MSTIDs in Figures 7e and 7f can be confirmed indirectly by the orthogonal propagation direction observed by previous researches (Shiokawa, Ihara, et al., 2003; Tsugawa, Kotake, et al., 2007). Limited by the observable region, the analysis results of extension length (Figures 7c and 7d) and total area (Figures 7g and 7h) of MSTIDs might be less than their true scale where previous researches suggest that MSTIDs can extend up to 2,000 km (Tsugawa, Otsuka, et al., 2007; Yokoyama & Hysell, 2010). Similar with previous researches for daytime (Frissell et al., 2014, 2016) and nighttime (Lakshmi Narayanan et al., 2014) MSTIDs, we find that the mean value μ and the maximum likelihood value η of continuous characteristic distributions do not coincide, which can explain the difference of observed values in this research and previous observations (Huang et al., 2018) because the characteristic value, which is far away from the maximum likelihood value η, is more difficult to be observed and is always regarded as the statistical error in previous observations (Huang et al., 2018) but is calculated into the average in this research.

6. Discussion

To clarify the diurnal, seasonal and solar activity dependence of MSTID occurrence rate, the occurrence heatmap with a horizontal axis as month and a vertical axis as local time (LT) is shown in Figure 8 under high (annually averaged $F_{10.7}$ are 128.45 and 122.67 in 2003 and 2013, respectively) and low (annually averaged $F_{10.7}$ are 74.07 and 69.93 in 2008 and 2018, respectively) solar activity conditions. The same diurnal and seasonal dependence with previous researches are revealed that nighttime MSTIDs have a maximum occurrence rate around summer solstice for nearly 100% at 21–3 LT (Kotake et al., 2006) and a secondary maximum in winter at 19–23 LT from December to February (Otsuka et al., 2021), whereas daytime MSTIDs have a maximum around winter solstice at 9–15 LT (Kotake et al., 2006) and a secondary maximum after summer sunrise at 6–9 LT from June to August (Otsuka et al., 2021). However, the solar activity dependence of MSTID occurrence shown in this paper and Otsuka et al. (2021) is different. Results in Figure 8 suggest that in high solar activity year, occurrence rate is higher during the preference season with maximum occurrence of MSTIDs (e.g., 7–18 LT in winter from November to January for daytime MSTIDs and 19–6 LT in summer from May to July for nighttime MSTIDs) but lower during the occurrence non-preference season (e.g., 10–14 LT in spring from March to May for daytime MSTIDs and 20–4 LT in winter from January to February for nighttime MSTIDs), while previous research (Otsuka et al., 2021) suggests that the occurrence rate is higher all over the low solar activity year. One possible explanation for the different conclusions is that the dTEC data with a Kp index greater than four is excluded in research of Otsuka et al. (2021) but included in this research. This restriction may make the data unbalanced because more data is excluded in high solar activity year according to the positive correlation between solar and geomagnetic activities (Hajra et al., 2021).

In order to illustrate the external dependence of MSTID characteristics more intuitively, we calculate the monthly average shown in Figure 9a and annual average shown in Figure 9b to compare the variation of external factors (solar and geomagnetic activity indexes $F_{10.7}$ and Kp) and characteristics (occurrence rate, wavelength, extension direction, extension length, wavelike structure number and total area) of daytime/nighttime MSTIDs (red/blue curve). Besides, the seasonal dependence of MSTID characteristics can be confirmed by Figure 9a where yellow and green bars refer to summer (June to August) and winter (December to February), respectively.

6.1. Solar Activity Dependence

In terms of occurrence dependence for nighttime MSTIDs, our result suggests the same seasonal compounded correlation observed by Terra et al. (2020). The third panel of Figure 9a suggests that nighttime MSTID occurrence rate keeps a positive/negative correlation with solar activity around summer/winter solstice (June/December), respectively, leading to a larger peak-to-valley variation of occurrence rate within a higher solar activity year. Thus it is inaccurate to describe the solar activity dependence of MSTID occurrence from the perspective of annual average because the negative correlation shown in the third panel of Figure 9b is almost the same with that of Otsuka et al. (2021), where 22-year MSTIDs over Japan are discriminated from the same data set with a criterion of GPS-TEC variation $\Delta I / \bar{I} > 1\%$. In terms of occurrence dependence for daytime MSTIDs, occurrence

Annual Occurrence Heatmap of MSTIDs in Different Solar Activity Conditions
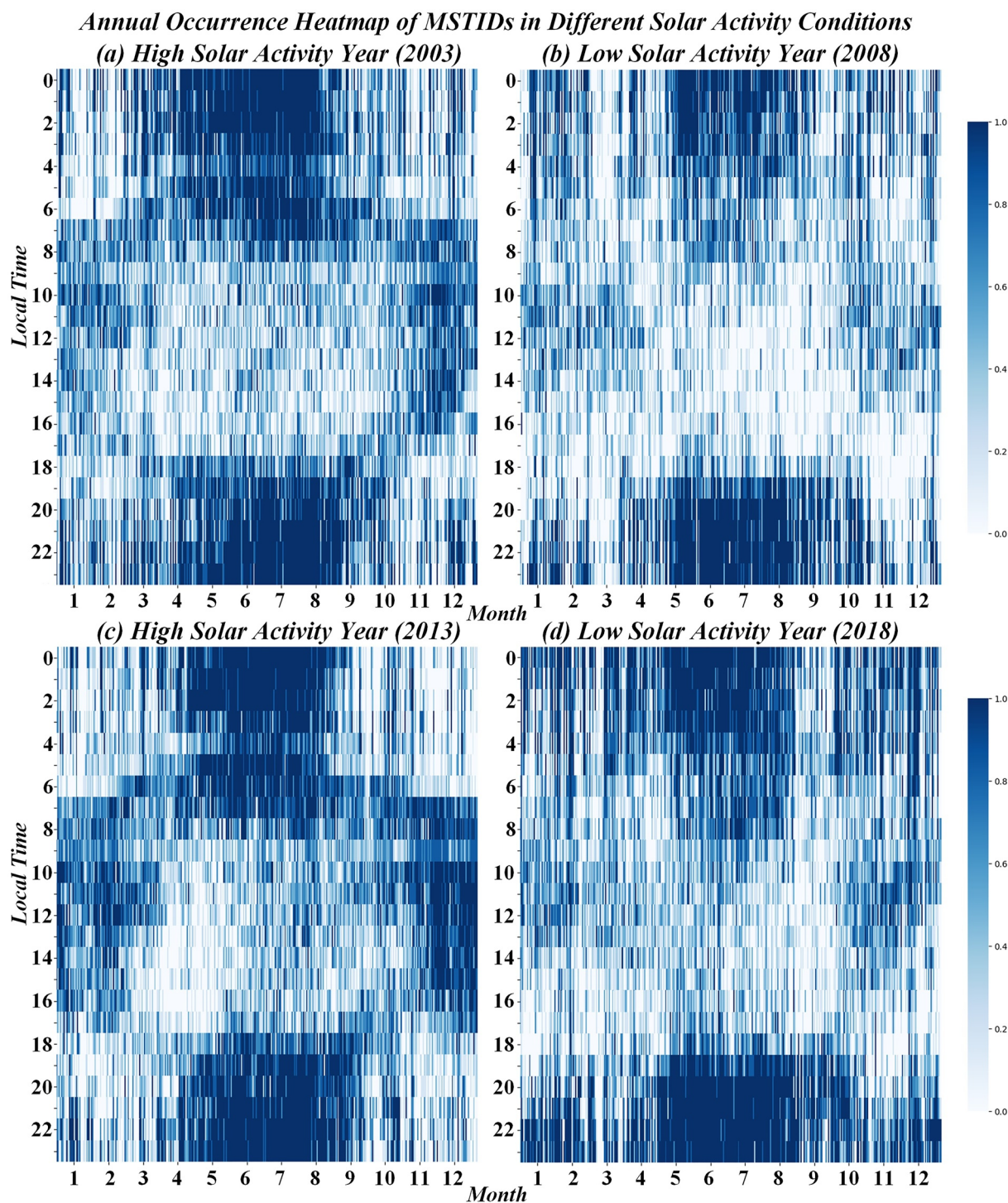
Figure 8. The seasonal and diurnal distribution of Medium-scale traveling ionospheric disturbances (MSTID) occurrence result of this research in high (2003 and 2013) and low (2008 and 2018) solar activity. Since 6 frames of detrended TEC (dTEC) maps are obtained every hour, the color scale represented for occurrence rate ranges from 0 to 1 with an interval of 1/6. A thicker color refers to a higher occurrence rate.

rate in winter and peak-to-valley variation are also larger when the solar activity is higher except December 2001 according to the third panel of Figure 9a. One possible explanation for this abnormality is that TEC perturbations are so severe that the detrended window of dTEC maps need to be less than 1 hr to filter out all long-term

AGU
ADVANCING EARTH
AND SPACE SCIENCE

Space Weather

10.1029/2022SW003151
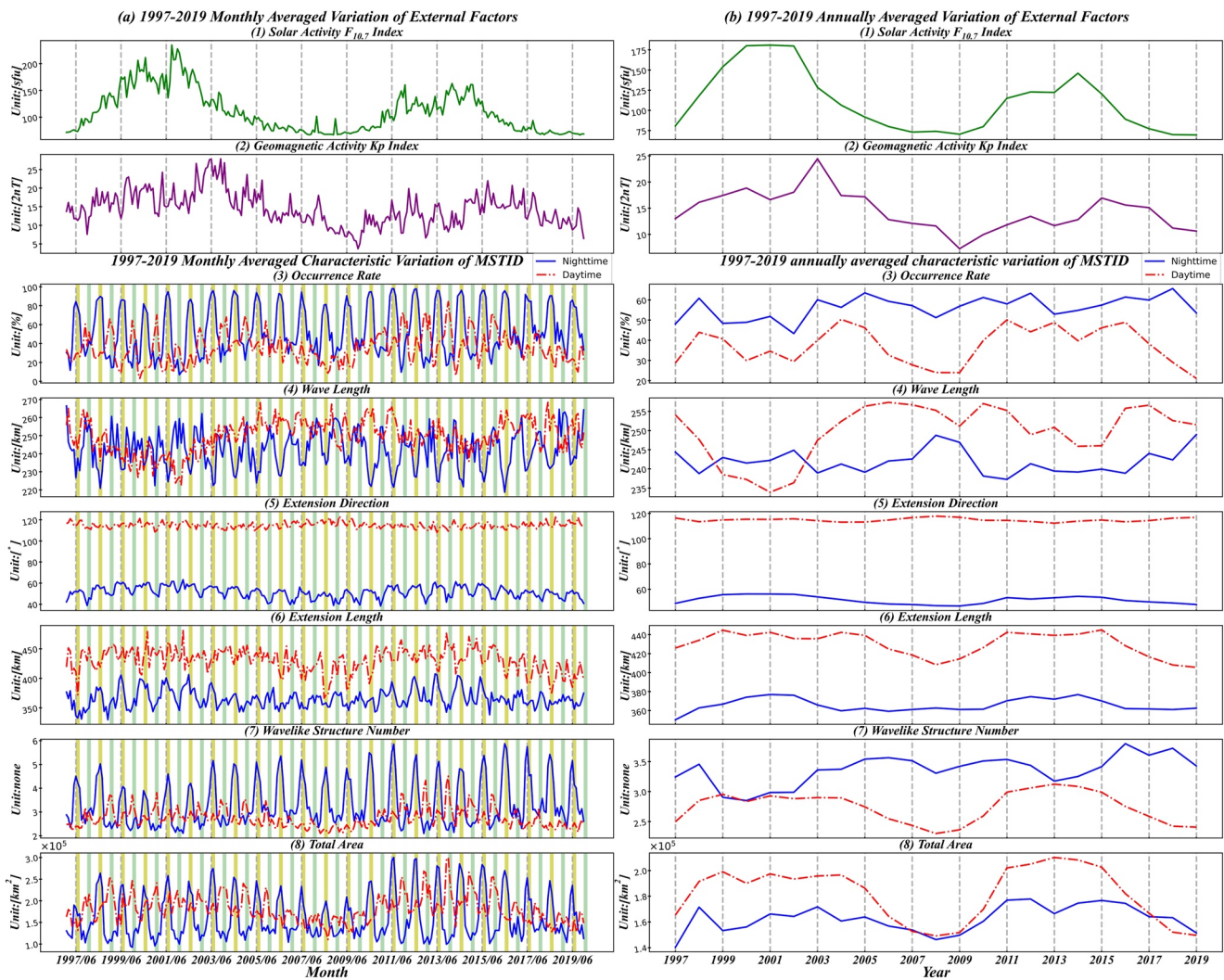
Figure 9. Monthly (a) and annually (b) averaged variation of external factors: (1) solar activity $F_{10.7}$ index and (2) geomagnetic activity Kp index; variation of daytime/nighttime (red/blue curve) Medium-scale traveling ionospheric disturbance (MSTID) characteristics: (3) occurrence rate, (4) wavelength, (5) extension direction, (6) extension length, (7) wavelike structure number and (8) total area. Yellow and green bars in subplot (a) refer to summer (June to August) and winter (December to February), respectively.

variations. There are more non-wavelike perturbations at daytime, which is regarded as the reason why daytime occurrence rate curve of Otsuka et al. (2021) is different from ours.

Terra et al. (2020) explain the seasonal compounded solar activity dependence of MSTID occurrence by the thermospheric neutral wind which has a northeastern (northwestern) acceleration ($\textit{\textbf{a}}$ in $ms^{-1}F_{10.7}^{-1}$) in northern hemisphere summer (winter) night (Brum et al., 2012; Emmert et al., 2006), which is favorable (unfavorable) for Perkins instability growth of nighttime MSTIDs. On the other hand, viscosity effect, which reduces the amplitude of gravity waves, is a possible explanation for positive solar activity correlation for annually averaged occurrence rate of daytime MSTIDs shown in the third panel of Figure 9b because viscosity effect increases as the decrease of solar activity due to the decrease of neutral density (Vadas, 2007).

According to the fourth panel of Figure 9b, horizontal wavelength of nighttime MSTIDs keeps negative correlation with solar activity, which is consistent with the wavelength variation in China (Huang et al., 2018). The physical explanation for this dependence needs further study because there is no variable term for wavelength in the growth rate of Perkins instability (Perkins, 1973). In terms of physical explanation for negative correlation of daytime MSTID wavelength, previous simulation has showed that it is difficult for gravity waves with shorter wavelength to propagate to the higher altitudes when the thermospheric temperature is low (Vadas, 2007).

Space Weather

10.1029/2022SW003151

Considering the thermospheric temperature has positive correlation with solar activity, gravity waves with larger horizontal wavelength can propagate into the thermosphere more easily during the solar minimum period.

The long-term observation of extension direction was few but can be indirectly confirmed by propagation direction because they are orthogonal to each other. Previous researches of propagation direction (Hernández-Pajares et al., 2012; Otsuka et al., 2021) showed the similar variation trend after transforming to extension direction in the same coordinate of this research. The positive correlation in nighttime ($r' = 0.928$) and the stabilization in daytime ($r' = 0.361$) in this research shows a good agreement with theirs.

The seventh panel of Figure 9a shows that wavelike structure number of nighttime MSTIDs decreases when solar activity $F_{10.7}$ exceeds about 130 sfu, while daytime MSTIDs show positive correlation. The cause of this phenomenon of nighttime MSTIDs may contribute to the saturation of neutral wind speed for solar activity at $F_{10.7} = 140–160$ sfu observed from American sector (Brum et al., 2012; Emmert et al., 2006) and Asian sector (Liu et al., 2004), because the neutral wind may play an important role in the generation of polarization electric field (Shiokawa, Otsuka, et al., 2003). However, the extension length has a positive correlation with solar activity in the sixth panel of Figure 9b, so that the total area of MSTIDs still shows positive solar activity correlation in the eighth panel of Figure 9b.

6.2. Geomagnetic Activity Dependence

Similar to previous researches (Evans et al., 1983; Georges, 1968; Morton & Essex, 1978), the partial correlation analysis of this research ($|r'_{C \cdot Kp/F_{10.7}}| < 0.4$ shown in Table 2) also shows that the characteristics of MSTIDs have no obvious correlation with geomagnetic activity after eliminating the influence of solar activity.

Previous researches that derived positive (Bristow & Greenwald, 1996) or negative (Ding et al., 2011) correlation with geomagnetic activity could fall into the category of event analysis or short-term analysis without generality. In terms of long-term analyses, the research that concludes negative correlation (Seker et al., 2011) only derived the correlation coefficient between MSTID characteristics and geomagnetic activity without eliminating the influence of solar activity. The observation of Terra et al. (2020) shows the positive correlation after eliminating the influence of solar activity during 2018–2019 solar minimum period when the geomagnetic activity is low ($Kp < 4$), whereas the observation of Saito et al. (2001) suggests no obvious correlation in night days of solar minimum year with a higher geomagnetic activity ($\Sigma Kp = 11–22$).

6.3. Seasonal Dependence

Except for wavelength (Shiokawa, Ihara, et al., 2003), seasonal dependence of other characteristics are synchronous with occurrence rate shown in Figure 9a. The MSTID occurrence preference is the same as previous researches (Ding et al., 2011; Kil & Paxton, 2017), where daytime MSTIDs have a maximum occurrence rate in winter and a secondary maximum in summer, whereas nighttime MSTIDs have a maximum in summer and a secondary maximum in winter. The secondary maximums of occurrence rate, which are relatively low compared with the maximums, are omitted in some previous researches (Hernández-Pajares et al., 2006; Jacobson et al., 1995).

The neutral density variation in the thermosphere and vertical temperature gradient in the mesosphere can explain the maximum and the secondary maximum occurrence rate of daytime MSTIDs around winter and summer solstices, respectively. These two peaks are produced because the density in thermosphere reaches to minimum at the solstices which makes it easier for propagation of gravity waves (Moore & Boulton, 1987). Compared with summer peak, the peak in winter is higher because more gravity waves near the mesopause is reflected instead of propagating upward due to the steeper temperature gradient in summer (Bristow et al., 1996).

As for the seasonal dependence of nighttime MSTIDs, our result also shows the maximum and the secondary maximum occurrence rate in summer and winter solstices, respectively, as presented by previous observation (Kotake et al., 2006; Martinis et al., 2010; Tsugawa, Kotake, et al., 2007), but the secondary maximum in winter is relatively low unlike daytime MSTIDs (Ding et al., 2011). Perkins instability can explain these peaks: because the growth rate of a Perkins instability is inversely proportional to the neutral density (Perkins, 1973) which decreases to the minimum around summer and winter solstices but lowest around the summer solstice (Moore & Boulton, 1987).

Polarization electric field coupling can explain the seasonal occurrence preference of nighttime MSTIDs in another aspect. Previous researches have found that ionospheric perturbations in the E region over Japan have a maximal occurrence rate in summer (Narayanan et al., 2018). According to the inter-layer coupling mechanism (Yokoyama & Hysell, 2010), the nighttime MSTID occurrence also reaches maximum in summer. When the occurrence rate of nighttime MSTIDs in Australia, with the same longitude and conjugated geomagnetic latitude, reaches maximum in local summer, according to inter-hemispheric conjugation mechanism (Otsuka et al., 2004), there should be a secondary maximum of occurrence rate during local winter over Japan (Martinis et al., 2010).

7. Summary

In this research, we propose the first MSTID processing algorithm based on deep learning instance segmentation Mask R-CNN model which can detect wavelike perturbations intelligently and derive characteristics automatically from 1997 to 2019 up to 1,209,600 dTEC maps with an accuracy of about 80% and a real-time processing speed of about 8 fps in different circumstances. Then wavelike perturbations are normalized by circumscribed ellipses and the spatial information of them is stored in a characteristic matrix. To avoid the situation that a wavelike structure in the characteristic matrix is denied to be a part of MSTIDs just because of one large characteristic value, the nonlinear optimization tool is used to determine the threshold of the filtering criterion which eliminates the isolated wavelike perturbations to obtain MSTID characteristics. The effectiveness of this algorithm is evaluated from two aspects of detection performance for wavelike perturbation and filtering criterion performance for isolated wavelike perturbation elimination.

The statistical analysis for MSTID characteristics derived by above algorithm is carried out from probability distribution and time-series variation aspects which are corresponding to existing observations. The hourly updated MSTID characteristic database reveals the external factor dependence including season, solar and geomagnetic activity. In terms of solar activity dependence, our results clarify that solar activity dependence of MSTID occurrence is seasonally compounded in the monthly average whereas the annual average shows simple negative (positive) correlation for nighttime (daytime) MSTIDs. In terms of geomagnetic activity dependence, the partial correlation coefficients of all characteristics which can eliminate the influence of solar activity $|r'_{C \cdot K_p / F_{10.7}}| < 0.4$ indicates there is no obvious correlation between MSTID characteristics and geomagnetic activity. In terms of seasonal dependence, the result of this research also shows the same conclusions with existing observations that the preference season of MSTID occurrence is around summer and winter solstices. Moreover, the possible physical explanations for these dependence are also given in this research.

This first real-time MSTID processing and analyzing method based on the artificial intelligence can be integrated into the existing dTEC observation system, which is expected to contribute to the industrial deployment such as space weather forecast and quality improvement of satellite communication.

Data Availability Statement

The dTEC maps are available in NICT: https://aer-nc-web.nict.go.jp/GPS/GEONET/MAP/. The instance segmentation model Mask R-CNN and annotation tool *Labelme* are open-sourced software in Zenodo or Github: https://doi.org/10.5281/zenodo.6776091 and https://doi.org/10.5281/zenodo.5711226, respectively. Solar activity index $F_{10.7}$ is retrieved from Goddard Space Flight Center of NASA: https://omniweb.gsfc.nasa.gov/form/dx1.html. Geomagnetic activity index Kp is derived from GFZ Helmholtz Centre: https://www.gfz-potsdam.de/en/kp-index/.

References

Bristow, W. A., & Greenwald, R. A. (1996). Multiradar observations of medium-scale acoustic gravity waves using the super dual auroral radar network. *Journal of Geophysical Research*, *101*(A11), 24499–24511. https://doi.org/10.1029/96JA01494

Bristow, W. A., Greenwald, R. A., & Villain, J. P. (1996). On the seasonal dependence of medium-scale atmospheric gravity waves in the upper atmosphere at high latitudes. *Journal of Geophysical Research*, *101*(A7), 15685–15699. https://doi.org/10.1029/96JA01010

Brum, C. G. M., Tepley, C. A., Fentzke, J. T., Robles, E., dos Santos, P. T., & Gonzalez, S. A. (2012). Long-term changes in the thermospheric neutral winds over Arecibo: Climatology based on over three decades of Fabry-Perot observations. *Journal of Geophysical Research*, *117*(A2). https://doi.org/10.1029/2011JA016458

Calais, E., & Minster, J. B. (1995). Gps detection of ionospheric perturbations following the January 17, 1994, Northridge earthquake. *Geophysical Research Letters*, *22*(9), 1045–1048. https://doi.org/10.1029/95GL00168

Chinchor, N. (1992). Muc-4 evaluation metrics. In *Proceedings of the 4th conference on message understanding* (pp. 22–29). Association for Computational Linguistics. https://doi.org/10.3115/1072064.1072067

Ding, F., Wan, W., Xu, G., Yu, T., Yang, G., & Wang, J.-s. (2011). Climatology of medium-scale traveling ionospheric disturbances observed by a GPS network in central China. *Journal of Geophysical Research*, *116*(A9). https://doi.org/10.1029/2011JA016545

Ding, F., Yuan, H., Wan, W., Reid, I. M., & Woithe, J. M. (2004). Occurrence characteristics of medium-scale gravity waves observed in oh and oi nightglow over adelaide (34.5°S, 138.5°E). *Journal of Geophysical Research*, *109*(D14), D14104. https://doi.org/10.1029/2003JD004096

Ellett, F. S., & Ericson, D. P. (1986). Correlation, partial correlation, and causation. *Synthese*, *67*(2), 157–173. https://doi.org/10.1007/bf00540066

Emmert, J. T., Faivre, M. L., Hernandez, G., Jarvis, M. J., Meriwether, J. W., Niciejewski, R. J., et al. (2006). Climatologies of nighttime upper thermospheric winds measured by ground-based Fabry-Perot interferometers during geomagnetically quiet conditions: 1. Local time, latitudinal, seasonal, and solar cycle dependence. *Journal of Geophysical Research*, *111*(A12), A12302. https://doi.org/10.1029/2006JA011948

Evans, J. V., Holt, J. M., & Wand, R. H. (1983). A differential-Doppler study of traveling ionospheric disturbances from millstone hill. *Radio Science*, *18*(3), 435–451. https://doi.org/10.1029/RS018i003p00435

Frissell, N. A., Baker, J., Ruohoniemi, J. M., Gerrard, A. J., Miller, E. S., Marini, J. P., et al. (2014). Climatology of medium-scale traveling ionospheric disturbances observed by the midlatitude blackstone superdarn radar. *Journal of Geophysical Research: Space Physics*, *119*(9), 7679–7697. https://doi.org/10.1002/2014JA019870

Frissell, N. A., Baker, J. B. H., Ruohoniemi, J. M., Greenwald, R. A., Gerrard, A. J., Miller, E. S., & West, M. L. (2016). Sources and characteristics of medium-scale traveling ionospheric disturbances observed by high-frequency radars in the North American sector. *Journal of Geophysical Research: Space Physics*, *121*(4), 3722–3739. https://doi.org/10.1002/2015JA022168

Garcia, F. J., Kelley, M. C., Makela, J. J., & Huang, C.-S. (2000). Airglow observations of mesoscale low-velocity traveling ionospheric disturbances at midlatitudes. *Journal of Geophysical Research*, *105*(A8), 18407–18415. https://doi.org/10.1029/1999JA000305

Georges, T. (1968). HF Doppler studies of traveling ionospheric disturbances. *Journal of Atmospheric and Terrestrial Physics*, *30*(5), 735–746. https://doi.org/10.1016/S0021-9169(68)80029-7

Girshick, R. (2015). Fast R-CNN, In *2015 IEEE International Conference on Computer Vision (ICCV)*, (pp. 1440–1448). https://doi.org/10.1109/ICCV.2015.169

Hajra, R., Marques de Souza Franco, A., Echer, E., & José Alves Bolzan, M. (2021). Long-term variations of the geomagnetic activity: A comparison between the strong and weak solar activity cycles and implications for the space climate. *Journal of Geophysical Research: Space Physics*, *126*(4), e2020JA028695. https://doi.org/10.1029/2020JA028695

He, K., Gkioxari, G., Dollár, P., & Girshick, R. (2017). Mask r-cnn. In *2017 IEEE international conference on computer vision (iccv)* (pp. 2980–2988). https://doi.org/10.1109/ICCV.2017.322

Hernández-Pajares, M., Juan, J. M., & Sanz, J. (2006). Medium-scale traveling ionospheric disturbances affecting GPS measurements: Spatial and temporal analysis. *Journal of Geophysical Research*, *111*(A7), A07S11. https://doi.org/10.1029/2005JA011474

Hernández-Pajares, M., Juan, J. M., Sanz, J., & Aragón-Àngel, A. (2012). Propagation of medium scale traveling ionospheric disturbances at different latitudes and solar cycle conditions. *Radio Science*, *47*(6). https://doi.org/10.1029/2011RS004951

Huang, F., Dou, X., Lei, J., Lin, J., Ding, F., & Zhong, J. (2016). Statistical analysis of nighttime medium-scale traveling ionospheric disturbances using airglow images and GPS observations over central China. *Journal of Geophysical Research: Space Physics*, *121*(9), 8887–8899. https://doi.org/10.1002/2016JA022760

Huang, F., Lei, J., Dou, X., Luan, X., & Zhong, J. (2018). Nighttime medium-scale traveling ionospheric disturbances from airglow imager and global navigation satellite systems observations. *Geophysical Research Letters*, *45*(1), 31–38. https://doi.org/10.1002/2017GL076408

Jacobson, A. R., Carlos, R. C., Massey, R. S., & Wu, G. (1995). Observations of traveling ionospheric disturbances with a satellite-beacon radio interferometer: Seasonal and local time behavior. *Journal of Geophysical Research*, *100*(A2), 1653–1665. https://doi.org/10.1029/94JA02663

Kil, H., & Paxton, L. J. (2017). Global distribution of nighttime medium-scale traveling ionospheric disturbances seen by swarm satellites. *Geophysical Research Letters*, *44*(18), 9176–9182. https://doi.org/10.1002/2017GL074750

Kotake, N., Otsuka, Y., Tsugawa, T., Ogawa, T., & Saito, A. (2006). Climatological study of GPS total electron content variations caused by medium-scale traveling ionospheric disturbances. *Journal of Geophysical Research*, *111*(A4), A04306. https://doi.org/10.1029/2005JA011418

Krizhevsky, A., Sutskever, I., & Hinton, G. E. (2012). Imagenet classification with deep convolutional neural networks. In F. Pereira, C. J. C. Burges, L. Bottou, & K. Q. Weinberger (Eds.), *Advances in neural information processing systems* (Vol. 25). Curran Associates, Inc. Retrieved from https://proceedings.neurips.cc/paper/2012/file/c399862d3b9d6b76c8436e924a68c45b-Paper.pdf

Lakshmi Narayanan, V., Shiokawa, K., Otsuka, Y., & Saito, S. (2014). Airglow observations of nighttime medium-scale traveling ionospheric disturbances from Yonaguni: Statistical characteristics and low-latitude limit. *Journal of Geophysical Research: Space Physics*, *119*(11), 9268–9282. https://doi.org/10.1002/2014JA020368

Lin, T.-Y., Dollár, P., Girshick, R., He, K., Hariharan, B., & Belongie, S. (2017). Feature Pyramid Networks for Object Detection, In *2017 IEEE Conference on Computer Vision and Pattern Recognition (CVPR)*, (pp. 936–944). https://doi.org/10.1109/CVPR.2017.106

Liu, L., Luan, X., Wan, W., Lei, J., & Ning, B. (2004). Solar activity variations of equivalent winds derived from global ionosonde data. *Journal of Geophysical Research*, *109*(A12), A12305. https://doi.org/10.1029/2004JA010574

Long, J., Shelhamer, E., & Darrell, T. (2015). Fully convolutional networks for semantic segmentation. In *2015 IEEE conference on computer vision and pattern recognition (CVPR)* (pp. 3431–3440). https://doi.org/10.1109/CVPR.2015.7298965

Makela, J. J., Miller, E. S., & Talaat, E. R. (2010). Nighttime medium-scale traveling ionospheric disturbances at low geomagnetic latitudes. *Geophysical Research Letters*, *37*(24). https://doi.org/10.1029/2010GL045922

Martinis, C., Baumgardner, J., Wroten, J., & Mendillo, M. (2010). Seasonal dependence of MSTIDs obtained from 630.0 nm airglow imaging at Arecibo. *Geophysical Research Letters*, *37*(11). https://doi.org/10.1029/2010GL043569

Mendillo, M., Baumgardner, J., Nottingham, D., Aarons, J., Reinisch, B., Scali, J., & Kelley, M. (1997). Investigations of thermospheric-ionospheric dynamics with 6300-Å images from the Arecibo observatory. *Journal of Geophysical Research*, *102*(A4), 7331–7343. https://doi.org/10.1029/96JA02786

Moore, P., & Boulton, W. (1987). Some aspects of a global thermospheric density model deduced from the analysis of the orbit of intercosmos 13 rocket (1975-22b). *Planetary and Space Science*, *35*(8), 1039–1052. https://doi.org/10.1016/0032-0633(87)90008-0

Morton, F., & Essex, E. (1978). Gravity wave observations at a southern hemisphere mid-latitude station using the total electron content technique. *Journal of Atmospheric and Terrestrial Physics*, *40*(10), 1113–1122. https://doi.org/10.1016/0021-9169(78)90059-4

Munro, G. H. (1950). Travelling disturbances in the ionosphere. *Proceedings of the Royal Society of London, Series A: Mathematical and Physical Sciences*, *202*(1069), 208–223. Retrieved from http://www.jstor.org/stable/98462

Narayanan, V. L., Shiokawa, K., Otsuka, Y., & Neudegg, D. (2018). On the role of thermospheric winds and sporadic E layers in the formation and evolution of electrified MSTIDs in geomagnetic conjugate regions. *Journal of Geophysical Research: Space Physics*, *123*(8), 6957–6980. https://doi.org/10.1029/2018JA025261

Otsuka, Y., Shinbori, A., Tsugawa, T., & Nishioka, M. (2021). Solar activity dependence of medium-scale traveling ionospheric disturbances using GPS receivers in Japan. *Earth Planets and Space*, *73*(1), 22. https://doi.org/10.1186/s40623-020-01353-5

京都大学
KYOTO UNIVERSITY

京都大学学術情報リポジトリ
KURENAI 紅
Kyoto University Research Information Repository

Space Weather

10.1029/2022SW003151

Otsuka, Y., Shiokawa, K., Ogawa, T., & Wilkinson, P. (2004). Geomagnetic conjugate observations of medium-scale traveling ionospheric disturbances at midlatitude using all-sky airglow imagers. *Geophysical Research Letters*, *31*(15), L15803. https://doi.org/10.1029/2004GL020262

Perkins, F. (1973). Spread F and ionospheric currents. *Journal of Geophysical Research*, *78*(1), 218–226. https://doi.org/10.1029/JA078i001p00218

Saito, A., Fukao, S., & Miyazaki, S. (1998). High resolution mapping of TEC perturbations with the GSI GPS network over Japan. *Geophysical Research Letters*, *25*(16), 3079–3082. https://doi.org/10.1029/98GL52361

Saito, A., Nishimura, M., Yamamoto, M., Fukao, S., Kubota, M., Shiokawa, K., et al. (2001). Traveling ionospheric disturbances detected in the front campaign. *Geophysical Research Letters*, *28*(4), 689–692. https://doi.org/10.1029/2000GL011884

Samson, J. C., Greenwald, R. A., Ruohoniemi, J. M., Frey, A., & Baker, K. B. (1990). Goose bay radar observations of earth-reflected, atmospheric gravity waves in the high-latitude ionosphere. *Journal of Geophysical Research*, *95*(A6), 7693–7709. https://doi.org/10.1029/JA095iA06p07693

Seker, I., Fung, S. F., & Mathews, J. D. (2011). Relation between magnetospheric state parameters and the occurrence of plasma depletion events in the nighttime midlatitude F region. *Journal of Geophysical Research*, *116*(A4). https://doi.org/10.1029/2010JA015521

Shiokawa, K., Ihara, C., Otsuka, Y., & Ogawa, T. (2003). Statistical study of nighttime medium-scale traveling ionospheric disturbances using midlatitude airglow images. *Journal of Geophysical Research*, *108*(A1), 1052. https://doi.org/10.1029/2002JA009491

Shiokawa, K., Otsuka, Y., Ihara, C., Ogawa, T., & Rich, F. J. (2003). Ground and satellite observations of nighttime medium-scale traveling ionospheric disturbance at midlatitude. *Journal of Geophysical Research*, *108*(A4), 1145. https://doi.org/10.1029/2002JA009639

Terra, P., Vargas, F., Brum, C. G. M., & Miller, E. S. (2020). Geomagnetic and solar dependency of MSTIDs occurrence rate: A climatology based on airglow observations from the Arecibo observatory ROF. *Journal of Geophysical Research: Space Physics*, *125*(7), e2019JA027770. https://doi.org/10.1029/2019JA027770

Tsugawa, T., Kotake, N., Otsuka, Y., & Saito, A. (2007). Medium-scale traveling ionospheric disturbances observed by GPS receiver network in Japan: A short review. *GPS Solutions*, *11*(2), 139–144. https://doi.org/10.1007/s10291-006-0045-5

Tsugawa, T., Otsuka, Y., Coster, A. J., & Saito, A. (2007). Medium-scale traveling ionospheric disturbances detected with dense and wide TEC maps over North America. *Geophysical Research Letters*, *34*(22), L22101. https://doi.org/10.1029/2007GL031663

Vadas, S. L. (2007). Horizontal and vertical propagation and dissipation of gravity waves in the thermosphere from lower atmospheric and thermospheric sources. *Journal of Geophysical Research*, *112*(A6). https://doi.org/10.1029/2006JA011845

Yin, F., Lühr, H., Park, J., & Wang, L. (2019). Comprehensive analysis of the magnetic signatures of small-scale traveling ionospheric disturbances, as observed by swarm. *Journal of Geophysical Research: Space Physics*, *124*(12), 10794–10815. https://doi.org/10.1029/2019JA027523

Yokoyama, T., & Hysell, D. L. (2010). A new midlatitude ionosphere electrodynamics coupling model (MIECO): Latitudinal dependence and propagation of medium-scale traveling ionospheric disturbances. *Geophysical Research Letters*, *37*(8). https://doi.org/10.1029/2010GL042598